npj 2D Materials and Applications

https://doi.org/10.1038/s41699-026-00664-7

Article in Press

Hexagonal boron nitride: interlayer with atomic scale precision for interface engineering in functional materials and devices

Received: 17 August 2025

Accepted: 7 January 2026

Cite this article as: Jung, J.-H., Kim, C.-J. Hexagonal boron nitride: interlayer with atomic scale precision for interface engineering in functional materials and devices. *npj 2D Mater Appl* (2026). https://doi.org/10.1038/s41699-026-00664-7

Ju-Hyun Jung & Cheol-Joo Kim

Hexagonal boron nitride: Interlayer with atomic scale precision for interface engineering in functional materials and devices

Ju-Hyun Jung[1], *Cheol-Joo Kim*[1,2,*]

[1]Department of Chemical Engineering, Pohang University of Science and Technology (POSTECH), Pohang 37673, Republic of Korea

[2]Center for Van der Waals Quantum Solids, Institute for Basic Science (IBS), Pohang 37673, Republic of Korea

[*]Corresponding author: kimcj@postech.ac.kr

ABSTRACT

Atomically thin hexagonal boron nitride (hBN) interlayers control interactions between electronic states of interfacing materials by modulating their separation at the atomic scale. These interlayers regulate interactions, whose strengths vary with distance. Here, we review how hBN is employed to enhance electronic and optoelectronic performance by mitigating disadvantageous interactions while preserving advantageous ones. Recent advances in hBN growth and integration are highlighted, and challenges that hinder widespread application are discussed.

Introduction

Heterostructures composed of dissimilar materials are at the heart of electronics and optoelectronics, offering functionalities beyond those of their individual components[1]. These functionalities arise from interfacial interactions, which modify both the electronic ground states at the interface and the dynamics of excited states. The strengths of various interlayer interactions depend strongly on the distance between interfacing materials and scale inversely with distance in distinct ways[2], governing emerging properties such as orbital hybridization[3], Coulombic coupling[4], and electronic tunneling[5]. Introducing insulating interlayers with precisely controlled thicknesses—acting as an effective electronic vacuum that physically separates adjacent materials—offers a promising strategy for engineering heterointerface properties by modulating these underlying mechanisms[6-10]. In particular, many interfacial interactions become negligible when the interlayer thickness exceeds a few nanometers. Thus, atomic-scale thickness control is essential for selectively modulating specific interactions to enhance targeted functionalities. Furthermore, uncontrolled interfacial defect states should be minimized to prevent disruption of these programmed interactions.

Such fine control is challenging to achieve with interlayer materials of non-layered structures. When these interlayers are deposited on a target surface, their formation is governed by specific surface chemistry through direct chemical bonds. As a result of island growth modes, non-uniform layers with pinholes and sub-nanometer thicknesses are often formed, leading to abundant atomic defects associated with dangling bonds on non-epitaxial substrates. In contrast, the thickness of layered insulators such as hexagonal boron nitride (hBN) can be precisely controlled at the atomic scale by adjusting the number of layers (N_L) (**Figure 1**). Moreover, its dangling-bond-free surface

facilitates the formation of pristine van der Waals (vdW) interfaces with various materials, enabling reliable modulation of key interfacial interactions and emergent properties[11-13].

In this review, we discuss the application of hBN as an interlayer in electronics and optoelectronics, focusing on how the thickness of hBN (t_{hBN}) influences interfacial interactions that govern charge and spin transport, as well as electric fields, both along and across various heterointerfaces. We also highlight recent approaches for fabricating atomically thin, single-crystal hBN interlayers and integrating them with other materials via sequential growth or transfer methods. Lastly, we outline current challenges in precise control of t_{hBN} and clean integration[14], along with promising strategies for hBN fabrication and integration.

Interface engineering with atomically thin hBN for electronics and optoelectronics

Modulation of interlayer interactions using atomically thin interlayer

Low-dimensional materials exhibit unique crystalline symmetries and electronic band structures, enabling novel properties. In these systems, reduced dimensionality suppresses intrinsic dielectric screening, making many-body interactions highly sensitive to the surrounding environment through non-local screening[15-17]. This environmental control can be captured quantitatively for two-dimensional (2D) materials by the Keldysh potential[18,19].

$$V(r) = \frac{e^2}{8\varepsilon_0 r_0}\left[H_0\left(\frac{r}{r_0}\right) - Y_0\left(\frac{r}{r_0}\right)\right], where\ r_0 = \frac{2\pi\chi_{2D}}{\varepsilon_{ave}} \quad (1)$$

where χ_{2D} is the 2D polarizability and ε_{ave} is the average dielectric constant of the media above and below the 2D layer, and H_0 and Y_0 denote the Struve and second-kind Bessel functions, respectively. Unlike in bulk, here ε_{ave} from the environment affects the screening length, r_0, and consequently, the strength of Coulomb interactions.

This sensitivity governs correlated and collective phenomena—including band-gap renormalization[20-22], superconductivity[23,24], Mott insulating behavior[25,26], and excitonic effects[21,22,27-29]—by tuning electron–electron and electron–hole interactions. For excitons, the binding energy follows a simple scaling, $E_b = E_{b0} \cdot \varepsilon_{ave}^{-\gamma}$ based on the effective Coulomb potential, where E_{b0} is the exciton binding energy in vacuum and γ is a scaling factor. With $\gamma \approx 0.7$ for monolayer MoS_2[30], this predicts that E_b for A exciton drops from 860 meV in vacuum to 455 meV on SiO_2 (ε_{ave}~2.5), and even adding a graphene overlayer on 2D semiconductors can reduce E_b by several hundred meV[22]. Considering that low-dimensional materials must be integrated with other components to form functional devices, such tunability underscores the importance of engineering the dielectric environment.

For cases where strong many-body interactions are desirable—such as in light-emitting diodes for enhanced luminescence[31] or excitonic devices[32]—vacuum provides a low ε, but introduces extrinsic disorder through adsorbates and oxidation of the low-dimensional materials[33], making device fabrication challenging. hBN, with its low ε (out-of-plane ε ~3–4, in-plane ε ~4–5), offers a chemically inert and atomically flat interface that suppresses dielectric disorder and charge inhomogeneities[16,34], making it an ideal passive component to preserve the suppressed dielectric screening of low-dimensional materials. Consequently, hBN has been widely employed as both a dielectric substrate and a passivating layer for various functional and quantum devices[35].

In contrast, there are cases where significantly enhanced Coulomb interactions within a material are desirable to enable emergent properties that are absent in its intrinsic form[36,37]. While it is essential to place the host material in close proximity to external materials that give rise to proximity effects, direct contact between the two often results in unwanted orbital hybridization and surface reconstruction, which can suppress the targeted properties. From this perspective, atomically thin hBN layers can be inserted between low-dimensional materials and screening materials, enabling control of proximity effects through the precise tuning of t_{hBN}. For example, first-principles calculations have shown a proximity-induced exchange coupling in which ferromagnetic Co or Ni induces a sizable exchange splitting in graphene through hBN spacers (≈10 meV for a single hBN layer), with the strength and sign of this exchange field tunable by the number of hBN layers[38]. This strategy can be applied to engineer various proximity-induced effects, such as spin–orbit coupling[39], magnetic exchange interactions[38], and superconducting correlations[40]. We also note that even when two materials must be in direct contact to realize proximity effects[41,42], hBN layers remain valuable as ultra-flat substrates and encapsulation layers, protecting heterointerfaces from environmental degradation that can obscure the desired effects.

The insulating hBN interlayers, with a large band gap of ~6 eV, can mediate not only electric fields but also charge transfer across the interface, serving as tunnel barriers. Because quantum tunneling is highly sensitive to t_{hBN}, decaying exponentially across the interlayer[43], hBN is typically used as a tunnel barrier in a much thinner regime than when it is employed as a dielectric medium—often at sub-nanometer thicknesses. In this ultra-thin regime, N_L-tunable hBN layers provide highly precise control over tunneling currents. Experimentally, the tunneling current across hBN has been shown to decrease by nearly two orders of magnitude for each additional monolayer ($t_{hBN} \approx 0.33$ nm)[5,44]. To compare hBN with other representative dielectric interlayer materials, **Table 1**

summarizes candidates used in 2D or 2D/3D heterostructures, outlining their dielectric constants, advantages, and limitations. More detailed examples of the applications will be discussed in the following sections.

Applications of thickness-controlled hBN interlayer

hBN interlayer for nanoelectronics

Atomically thin hBN interlayers offer precise control over interfacial interactions in 2D nanoelectronics, enabling the selective tuning of electronic coupling across critical interfaces[45]. In the semiconductor channel, one of the central challenges is balancing efficient doping with minimal mobility loss from Coulomb scattering. Conventional substitutional doping introduces ionized impurities directly into the channel, degrading mobility via impurity scattering. Remote doping with hBN interlayers addresses this by physically separating dopants from the channel, enabling carrier injection while exponentially suppressing Coulomb scattering, with the scattering potential, $\phi \propto e^{-qd}$, where d is t_{hBN}[4]. However, increased separation also reduces tunneling probability, diminishing doping efficiency (**Figure 2a**). Experiments show that, under a fixed dopant concentration, a channel with t_{hBN} = 2 nm exhibits higher carrier mobility than one with t_{hBN} = 1 nm (**Figure 2b**, yellow box), but its average carrier density decreases from 6.46×10^{12} to 3.32×10^{12} cm^{-2}—nearly a factor of two[4]. This result demonstrates that only with precise tunability of t_{hBN} via $N_{L,}$ the balance between Coulomb scattering suppression and sufficient charge transfer can be optimized.

Beyond the semiconductor channel/dielectric interface, the metal/semiconductor (M/S) interface is a key interface, whose properties are also governed by short-range interfacial interactions. High

contact resistance remains a critical challenge in 2D semiconductor devices, as direct metal deposition often induces metal-induced gap states (MIGS), associated with Fermi-level pinning[10,46,47]. In an ideal M/S junction, the Schottky barrier height, Φ_{SB} follows the Schottky–Mott limit (**Figure 2c**, left), determined by the difference between the metal work function, Φ_m and the semiconductor electron affinity, χ[48]. In practice, however, the metal wavefunction can penetrate into the semiconductor bandgap, creating MIGS that pin the Fermi level at a specific energy and increase Φ_{SB} (**Figure 2c**, middle) [46]. Introducing an atomically thin hBN interlayer between the metal and semiconductor (**Figure 2c**, right) [49,50] suppresses wavefunction penetration, thereby reducing MIGS formation and enabling Fermi-level depinning.

Density functional theory (DFT) calculations show that when the gap between a metal (Ni) and semiconductor (MoS_2) is less than 3 Å—comparable to the thickness of monolayer hBN—MIGS appear within the bandgap of MoS_2 (**Figure 2d**) [51]. In contrast, when the gap exceeds 5 Å, the projected density of states decreases significantly, leading to the elimination of MIGS. This result suggests that an hBN interlayer thicker than a bilayer (~6.6 Å) is required to effectively suppress Fermi-level pinning. However, because tunneling conductance decreases exponentially with t_{hBN}, excessively thick hBN layers can increase contact resistance. Therefore, t_{hBN} must be precisely controlled to suppress MIGS while maintaining tunneling efficiency in M/S junctions.

A similar trade-off arises in magnetic tunnel junctions (MTJs), where the interlayer distance, d governs spin-dependent tunneling and determines the tunneling magnetoresistance (TMR). Specifically, if the interlayer is too thin, spin-degenerate states can occur and tunnel through the barrier, reducing spin filtering and degrading TMR. Conversely, if the interlayer is too thick, the tunneling probability decreases, leading to high tunneling resistance and reduced TMR due to suppressed electron transport.

In the Ni/monolayer hBN/Ni MTJ, hybridization between the N p_z orbitals of hBN and the Ni d_z^2 orbitals results in metallic conduction, which reduces spin-filtering efficiency and TMR (**Figure 2e**, left) [3]. In contrast, when a bilayer hBN is introduced, orbital decoupling occurs between the Ni electrodes and the hBN interlayer, and electron transport occurs primarily via tunneling (**Figure 2e**, middle). This leads to increased spin-selective tunneling and a corresponding increase in TMR. However, TMR reaches a maximum of ~60% for bilayer hBN and then gradually decreases with further increases in t_{hBN} (**Figure 2e**, right), as confirmed by DFT simulations (**Figure 2f**) [52].

The control of interlayer thickness to mitigate disadvantageous interlayer interactions while preserving advantageous ones is a broadly applicable strategy for various electronic devices, as hBN interlayers with vdW surfaces allow versatile integration with a wide range of materials. Examples include tunneling devices for charge current[53,54], spin current[55], superconducting currents[56], and excited photo-carriers[57,58].

hBN interlayer for photonics and optoelectronics

Just as in nanoelectronics, precise thickness control of hBN is equally critical in optoelectronics, where optical and photonic responses are highly sensitive to interfacial conditions. For instance, in surface-enhanced Raman scattering (SERS), atomically thin hBN interlayers minimize substrate-induced perturbations and enable precise tuning of the near-field electromagnetic (EM) environment to maximize signal amplification. When incident light excites surface plasmon resonances in metals, intense local EM fields amplify Raman signals from analytes. However, conventional SERS substrates suffer from metal oxidation, spurious Raman peaks from metal–analyte bonding, and unwanted analyte conversion (**Figure 3a**) [59,60]. hBN passivation layers

mitigate these effects by suppressing oxidation, preventing direct metal–analyte bonding, and inhibiting photocatalytic reactions, as demonstrated by enhanced Raman signals from hBN-coated Au nanoparticles compared to uncovered regions (**Figure 3b,c**) [61].

The amplification factor is strongly dependent on t_{hBN} . Without hBN, poor EM field overlap between adjacent nanoparticles limits enhancement[59]. At an optimal thickness (t_{opt}), the hBN caps covering neighboring Au nanoparticles merge at their edges, forming a "double-hat" nanogap geometry that bridges the interparticle gap and concentrates the local EM field. In this configuration, two dome-like hBN surfaces facing each other form a valley-shaped cavity between the particles. This valley-like structure maximizes EM field overlap and produces intense SERS "hot spots" at the hBN surface. When the hBN becomes thicker, the merged caps flatten and field cancellation at the hBN surface reduces the enhancement (**Figure 3d**). Both finite-difference time-domain simulations and experiments confirm a thickness-dependent maximum in Raman amplification, followed by a decline at larger t_{hBN} (**Figure 3e,f**) [59]. Thus, hBN with its precise tunability in thickness serves as an ideal interlayer, blocking detrimental metal–analyte interactions while enhancing EM fields.

This strategy extends broadly to optoelectronic and photonic devices, including photonic memristors and single-photon emitters[62]. In vdW optoelectronics, monolayer transition-metal dichalcogenides (TMDs) exhibit direct band-to-band transitions, yielding strong photoluminescence (PL), and making them prime candidates for optoelectronic components based on vdW materials, ranging from light-emitting tunneling transistor to valleytronics. However, simply increasing the thickness does not proportionally enhance light emission, because multilayer or bulk counterparts revert to an indirect bandgap with strongly quenched PL[63]. Molecular intercalation has been utilized to decouple adjacent TMD layers by expanding the vdW gap,

resulting in stacks of TMDs with direct band gap features[64]. However, it suffers from nonuniform coverage and chemical instability, and its reproducibility remains limited due to the uncontrolled insertion of organic species and residual contamination within the vdW gap[65]. These limitations underscore the need for a clean, atomically thin spacer that can electronically isolate neighboring layers while preserving their intrinsic monolayer properties.

Incorporating an hBN interlayer between monolayer TMDs increases the interlayer distance and suppresses interlayer hybridization, thereby preserving the direct-gap electronic structure of individual layers. In this configuration, the spatial separation, further promotes Förster-type energy transfer between adjacent layers, enhancing the overall PL intensity (**Figure 3g**) [66]. These hBN-mediated heterostructures, composed of stacked WS_2/hBN unit cells, exhibit strong PL comparable to that of isolated monolayers, which further increases with the number of stacked units, indicating suppression of interlayer hybridization (**Figure 3h**) [67]. Notably, the PL intensity can exceed the sum of individual WS_2 monolayers by optimizing t_{hBN}. The PL intensity in WS_2/hBN/WS_2 exhibits a nonmonotonic dependence on t_{hBN}, reaching a maximum—about seven times higher than that of monolayer WS_2—at an t_{opt} (**Figure 3i**) [66]. This behavior highlights that, beyond interlayer decoupling, efficient Förster-type energy transfer governs the PL enhancement, emphasizing the importance of optimizing t_{hBN}. Furthermore, hBN interlayers have also been employed to investigate interlayer exciton dynamics, where controlled interlayer separation enables systematic tuning of charge transfer rates and exciton lifetimes in TMD heterostructures[68,69].

The hBN interlayer also regulates carrier transport in optoelectronic devices such as photodetectors and light-emitting devices, determining how efficiently carriers are injected, blocked, or recombined across the heterointerface. Acting as an atomically thin tunnel barrier, hBN enables

precise control of tunneling probability through its thickness, thereby balancing carrier blocking and transport essential for efficient photoresponse and light emission.

In MoS_2/hBN/graphene photodetectors, photons absorbed in MoS_2 generate electron-hole pairs, and the photoexcited holes tunnel through the hBN interlayer toward graphene (**Figure 4a**)[70]. This selective hole tunneling arises from asymmetric barrier heights, making hole transport dominant under illumination (**Figure 4b**). Consequently, t_{hBN} governs the trade-off between dark-current suppression and photocurrent generation (**Figure 4e**). When t_{hBN} is smaller than t_{opt}, carriers in graphene and MoS_2 can readily tunnel even under dark conditions, resulting in large leakage current and a low I_{ph}/I_{dark} ratio despite the relatively high photocurrent under illumination. However, increasing t_{hBN} beyond t_{opt} reduces tunneling probability, suppressing both dark and photocurrent. At $t_{opt,}$ the hBN interlayer blocks dark-carrier conduction while allowing photoexcited holes to tunnel through, yielding a high on/off ratio (**Figure 4c**).

In light-emitting tunneling devices based on WSe_2 (**Figure 4d**), electrons and holes are injected from opposite graphene electrodes through the hBN interlayer and radiatively recombine within the WSe_2 layer[57]. The t_{hBN} determines the tunneling balance that governs light emission efficiency. When the hBN interlayer is too thin, excessive carrier injection leads to strong leakage current and reduced electroluminescence efficiency due to non-radiative recombination (**Figure 4e**, left). Conversely, a too-thick interlayer suppresses carrier tunneling, which prolongs the carrier lifetime and can improve the internal quantum efficiency, but the reduced current density lowers the brightness of the emitted light (**Figure 4e**, right). These behaviors are consistent with the current–voltage characteristics, where the tunneling current decreases exponentially with increasing t_{hBN} (**Figure 4f**). Although this study does not present experimental data on t_{opt}, it is stated that 2–3 layers of hBN provide an optimal compromise between overall brightness and light-emission

efficiency of the devices. To more clearly illustrate the role of t_{hBN}, **Table 2** summarizes representative use cases of hBN interlayers, emphasizing how deviations from the t_{opt}—whether thinner ($t < t_{opt}$) or thicker ($t > t_{opt}$)—result in distinct interfacial and performance consequences.

Control of the thickness of hBN interlayers and integration

Many demonstrations of hBN interlayers have relied on exfoliated crystals, which lack precise t_{hBN} control and thus limit scalability to technologically relevant dimensions. Overcoming this requires a method to produce wafer-scale hBN films with atomic-level thickness precision. To grow such wafer-scale hBN films, various growth strategies have been developed, including chemical vapor deposition (CVD), molecular beam epitaxy (MBE), and metal–organic vapor phase epitaxy (MOVPE). Each method relies on distinct growth mechanisms and precursor chemistry; nevertheless, all exhibit trade-offs in achieving wafer-scale, single-crystalline, thickness-controlled hBN films.

Among these, CVD—in which volatile precursor compounds chemically react with other gases to produce a nonvolatile solid that deposits on a substrate—has become a widely adopted route for wafer-scale single-crystalline hBN films. Because reactant transport to and surface diffusion on the substrate occur uniformly, the process enables conformal epitaxial film growth without ultrahigh vacuum or complex beam-flux control. When transition-metal substrates are used for hBN growth, the growth involves catalytic decomposition of precursors on the metal surface, which lowers the activation energy for borazine ($B_3H_6N_3$) dehydrogenation[71] and thereby increases the deposition rate. However, the catalytic nature of the process also makes atomic-scale thickness control challenging, since the growth mode is governed by the surface reaction kinetics and the

solubility of B and N in the metal substrate. (Further details on CVD for atomic-scale thickness control are discussed later in this section.)

Unlike CVD, MBE directly supplies pure elemental boron and activated nitrogen species under ultrahigh vacuum (UHV, typically 10^{-9}–10^{-10} Torr). This configuration allows precise control of the incident atomic fluxes and enables growth of high-purity hBN films on non-catalytic substrates[72,73]. In MBE, film growth proceeds through the reaction of evaporated atomic or molecular beams with the crystalline substrate under controlled flux and temperature conditions. The epitaxial growth is achieved when adatoms can diffuse and incorporate into lattice sites before the next atoms arrive, so that previously adsorbed atoms have sufficient time to reach stable lattice (epitaxial lattice) positions before new atoms arrive and confine them in nonequilibrium positions, requiring a balance between surface diffusion and deposition rate. Because surface diffusion is thermally activated, the growth temperature must be sufficiently high to promote epitaxy, yet excessive heating can lead to desorption, which slows the deposition rate. Overall, MBE provides high purity and precise atomic flux control, but suffers from slow growth rate and difficulties in large-area deposition.

The use of metal-organic precursors in MOVPE is motivated by the intrinsically low vapor pressure and high melting point of elemental boron, which necessitate high process temperatures to ensure sufficient volatility for gas-phase transport during epitaxy. By forming organoborane compounds such as triethylborane ($B(C_2H_5)_3$, TEB) or trimethylborane ($B(CH_3)_3$, TMB), the boron source attains higher volatility and can be delivered in the gas phase with uniform flow and precise flux control[74]. In the presence of ammonia (NH_3), these precursors decompose thermally to generate reactive B–N species that adsorb on the substrate surface and form hBN layers. Owing to its gas-phase chemistry, MOVPE offers excellent uniformity, high reproducibility, and

compatibility with existing III–V platforms[75], enabling wafer-scale growth with controllable growth rates and precise composition control. Nonetheless, the decomposition of metal–organic precursors releases hydrocarbon by-products (e.g., C_2H_4, CH_4), and the residual alkyl ligands can lead to partial carbon incorporation into the hBN lattice[74], giving rise to turbostratic or polytype BN domains[76]. Recent optimization of precursor chemistry and growth conditions has significantly reduced carbon contamination and improved film uniformity, making MOVPE one of the most industrially scalable and commercially viable routes for high-quality hBN film growth.

Despite these advances, achieving simultaneous wafer-scale, single-crystalline, and atomic-scale thickness control remains a challenge. To address this, two main strategies have been pursued: (1) direct growth of multilayer hBN by tuning CVD growth conditions, and (2) layer-by-layer assembly of monolayers. In the first approach, CVD-based epitaxy on crystalline metals enables atomic-scale control of layer number. Metals such as Ni and Fe exhibit high B and N solubility, forming alloys during CVD that subsequently precipitate hBN upon cooling. The final thickness is governed by the amount of B and N dissolved in the metal, which can be tuned—within limits—by adjusting the flow rate of the gaseous precursor borazine ($B_3H_6N_3$) (**Figure 5a**) [77-79].

Uniform multilayer growth additionally requires controlling the interface where precipitation occurs. For example, on Ni substrates, crystalline Ni–B alloys form and drive a “synchronized growth” mechanism: hBN nuclei are edge-passivated by Ni–B, suppressing interlayer edge coalescence[77]. DFT calculations reveal that the Ni–B/Ni interfacial energy is high when the Ni–B layer is atomically thin (**Figure 5b**, top), favoring uniform multilayer growth to minimize the interfacial energy with a thicker Ni-layer (bottom). This mechanism implies that both the hBN nucleus and its edge-passivating Ni–B layer must be grown to precisely matched thicknesses. Experimentally, uniform trilayer hBN with wafer-scale uniformity has been achieved on Ni(111)

(**Figure 5c,d**), where the substrate's high surface energy appears to favor nucleation of a specific $t_{hBN} \sim 1$ nm[80].

While these results demonstrate uniform multilayer formation, the underlying mechanism for deterministic thickness control can be further explained by considering the thermodynamic aspects and growth conditions governing the hBN/Ni(111) interface. Deterministic control of t_{hBN} on Ni(111) arises from the t_{hBN}-dependent binding energy between hBN and the substrate, coupled with the growth-reaction equilibrium determined by borazine decomposition and H_2/N_2 coflow. DFT calculations show that the interfacial binding energy decreases significantly from monolayer to trilayer and then saturates for thicker films, creating distinct thermodynamic growth windows for bilayer, trilayer, and thicker hBN regimes. However, only bilayer, trilayer, and five-layer hBN films were realized, indicating that although multiple thermodynamic stability regimes exist in the thicker hBN regime, the kinetic growth window becomes too narrow for intermediate configurations such as four-layer and six-layer.

Experimentally, this behavior is consistent with the following growth conditions. Under 0.1 sccm borazine, H_2 = 10 sccm, and Ar = 10 sccm at 1220 °C, single-crystal trilayer hBN grows reproducibly. Reducing the precursor supply to 0.025 sccm borazine and increasing hydrogen to 20 sccm yields bilayer hBN. In contrast, introducing 50 sccm N_2 while maintaining 0.1 sccm borazine and H_2/Ar = 10/10 sccm drives the growth-reaction equilibrium ($B_3N_3H_6 + N_2 \rightleftharpoons$ hBN + B@Ni (B dissolved in Ni) + H_2) toward hBN formation, resulting in five-layer growth. These results show that the t_{hBN} can be quantitatively tuned by controlling precursor flux, which in turn modulates the chemical potential of H_2 and N_2 and thus the growth-reaction equilibrium, exploiting the intrinsic thermodynamic window defined by interfacial binding energies.

The second approach is sequential layer-by-layer assembly of monolayer hBN films grown in a surface-limited manner, with thickness defined by the number of layers, N_L. This requires mechanical exfoliation from the growth substrate without wet chemical processing, thereby avoiding contaminants that can alter the total thickness and introduce defect states detrimental to dielectric and tunneling properties. To enable this, the binding energy between the hBN film and the substrate, $\gamma_{hBN\text{-}substrate}$ must be lower than the vdW interactions between hBN layers, $\gamma_{hBN\text{-}hBN}$ (**Figure 5e**) [44,81]. Epitaxial growth on Ge(110) provides a model system: the substrate's weak interaction permits mechanical exfoliation (**Figure 5f**) [81]. Vicinal Ge(110) wafers with a miscut toward [001] present atomic step edges that direct unidirectional, single-crystalline monolayer growth, while their hydrogen-passivated surfaces further reduce interfacial binding below the vdW forces between hBN layers[81]. This allows vdW-mediated dry pick-up of hBN films without chemical treatments or polymer supports.

Formation of pristine interfaces with hBN

Once hBN interlayers are fabricated, the next step is to integrate them with other components to form interfaces with targeted functionalities. As discussed above, hBN interlayers enable selective modulation of interfacial interactions through atomic-scale thickness control. However, realizing such functional modulation requires not only precise thickness control but also the clean integration of additional crystalline layers on top and bottom of hBN interlayer (**Figure 1**). The same assembly techniques used to fabricate hBN films with controlled t_{hBN} can be extended to other material components, including both 2D and bulk materials[82]. For example, graphene grown epitaxially on Ge(110) can be mechanically assembled at the wafer scale with pristine interfaces

(**Figure 5g**) [44]. Using this approach, hBN/graphene superlattices have been fabricated with atomically clean interfaces, as confirmed by cross-sectional TEM imaging (**Figure 5h**).

While assembling individual components offers unprecedented versatility by decoupling the growth and integration processes—allowing hBN interlayers to be combined with a broad range of materials—Traditional transfer and assembly of van der Waals heterostructures typically require wet chemical etching of the growth substrate to release the 2D film before stacking. Such etching introduces polymer residues and metal contamination, while multiple manual transfer steps can generate interfacial bubbles, wrinkles, and induce mechanical stress[83]. In contrast, direct epitaxial growth of material A on hBN enables clean interface formation without chemical exposure. This eliminates polymer and etchant residues and minimizes mechanical deformation. Therefore, it is desirable to form the interfaces *in situ* during growth. For instance, when fabricating vertically stacked heterostructures in a sandwich-like configuration (A/hBN/B), where two distinct materials (A and B) are separated by an hBN interlayer, directly growing material A on an hBN interlayer with controlled t_{hBN} atop material B can eliminate one assembly step. This simplifies processing and avoids potential issues during assembly, such as strain-induced film deformation (**Figure 6a**).

Two relevant epitaxial growth strategies for achieving controlled interfaces between material A and hBN are remote epitaxy and van der Waals (vdW) epitaxy. Remote epitaxy leverages the atomic-scale thinness of hBN, which allows the field by charge polarity of the underlying substrate to permeate through the hBN layer, inducing epitaxial alignment in the deposited film (**Figure 6b**, top) [84]. As a result, the deposited film aligns crystallographically with the substrate, regardless of the hBN's own crystallinity (bottom). In contrast, vdW epitaxy exploits the weak vdW interactions between the film and hBN to guide crystallographic alignment (**Figure 6c**) [85]. Owing to these weak

interactions, epitaxially grown films can be mechanically exfoliated and transferred onto arbitrary surfaces to form vertical heterostructures without chemical etching (**Figure 6d**) [86]. For example, a GaAs film grown by remote epitaxy was exfoliated as a clean, 2-inch single-crystalline membrane (**Figure 6e**) with a root-mean-square surface roughness of ~0.40 nm, indicating clean exfoliation without damage (**Figure 6f**).

The advantages of direct growth extend beyond process simplification, offering precise control over atomic-scale interfacial structures. The thermodynamically driven interfacial configurations can give rise to novel interfacial electronic states[87,88]. For instance, DFT calculations show that introducing monolayer hBN into a MoS_2/Ni junction can significantly reduce Φ_{SB}, depending on how Ni is deposited[88]. Non-epitaxial deposition results in physisorption due to lattice mismatch, producing a large interlayer spacing and a small interface dipole (**Figure 6g**, left). In contrast, epitaxial deposition induces strong orbital hybridization, leading to chemisorption between Ni and hBN. Compared to physisorption, chemisorption decreases the interlayer distance and generates a stronger interface dipole (**Figure 6g**, right). This dipole creates a negative potential step ($\Delta V < 0$), lowering the Ni work function by ~1.8 eV and eliminating Φ_{SB} for electron transport (**Figure 6h**). Such interfacial engineering can be broadly applicable—from reducing contact resistance in transistors[87], to enhancing quantum efficiency in photocathodes[89], to increasing photoluminescence in perovskites[90]. These examples demonstrate that hBN is not merely a passive spacer but actively modulates interfacial states via dipole formation.

Challenges in hBN interlayer growth

While recent progress has enabled scalable growth and clean integration of hBN interlayers, several challenges remain. This section outlines four critical challenges in the development of large-area, high-quality hBN interlayers as follows (**Figure 7**).

Precise control of number of layers by direct growth

As mentioned, direct growth of hBN with controlled t_{hBN} is desirable. The N_L is controlled by adjusting growth time, precursor flux, and cooling rate on metal substrates with high B and N solubility. Despite some of advanced growth techniques, achieving arbitrary target thicknesses remains difficult. DFT calculations suggest that multilayer films with different thickness can have similar binding energies to the substrate, narrowing the growth window for selective thickness control[80]. Engineering growth substrates with extreme atomic-scale uniformity may be essential to overcoming this limitation, enabling both a uniform growth surface and a consistent edge-passivating layer for hBN. Furthermore, it is desirable to tune the B and N solubilities within the substrate itself, thereby suppressing precipitation beyond a target layer number. For example, graphene thickness on Si-doped Cu substrates can be tuned from one to four layers by regulating the saturation concentrations of carbon precursors[91]. Similarly, controlling the solubility of B and N in alloy catalysts may enable deterministic hBN thickness control by limiting precursor incorporation at the substrate.

Growth of wrinkle-free hBN

Wrinkle formation in CVD-grown hBN films is commonly caused by mismatch of thermal expansion between the film and substrate. During cooling, this mismatch induces internal stress, resulting in surface wrinkles[92] that degrade atomic flatness and introduce interfacial defects and scattering centers after integrations into device structures[93].

One approach to suppress wrinkles is to increase bonding strength between hBN and the metal substrate. For example, epitaxial growth on Cu–Ni alloy substrates results in stronger adhesion and flatter hBN films[93]. However, strong adhesion necessitates chemical etching during transfer for the integration of the hBN interlayer with other components, which prevents clean integration, while wrinkle formation persists on most other substrates—highlighting the need for a universal suppression strategy.

A promising alternative is hydrogen-plasma treatment after growth[94]. This process enables proton insertion at the substrate–film interface, relieving surface stress and eliminating wrinkles. Hydrogen-plasma treatment has been shown to suppress wrinkles in graphene via proton intercalation. If the hBN films, grown on such surface can be mechanically exfoliated, the approach is expected to be effective for providing a viable pathway for wrinkle-free, CVD-grown multilayer hBN interlayers[95].

Identifying the defect in hBN

CVD-grown hBN films typically exhibit higher leakage currents as tunnel barriers than mechanically exfoliated bulk hBN of the same thickness, indicating a higher density of defects[96,97]. Even epitaxially grown hBN contains structural defects, including point defects (e.g., B/N vacancies, substitutional impurities) and low-tilt-angle grain boundaries, which form when domains with the same orientation merge[98].

Atomic-level defect mapping requires high-resolution electron microscopy techniques such as scanning transmission electron microscopy (STEM), high-resolution TEM, and electron energy loss spectroscopy (EELS). For example, STEM-EELS has been used to visualize spatial distributions of vacancies, oxygen substitutions, and carbon impurities in monolayer hBN[99].

Applying these techniques to defect characterization and growth optimization could improve the crystal quality of CVD-grown hBN toward that of bulk hBN[35], thereby enabling its use in large-area device platforms. However, most studies on single-crystalline hBN layers lack detailed microstructural analysis to identify these defects, due to the low throughput and destructive nature of the characterization methods, making defect engineering in hBN more challenging.

To overcome these limitations, it is essential to understand the fundamental nature of point defects in hBN and the specific analytical demands involved in their identification. Point defects—such as vacancies and substitutional impurities—differ from the host lattice in both atomic arrangement and chemical composition. Identifying them requires atomic-scale resolution and chemical sensitivity, but direct observation is difficult in hBN due to its low atomic number contrast and the impracticality of performing such high-resolution analysis routinely across multiple samples.

To make defect characterization more accessible and scalable for growth optimization, a variety of non-destructive techniques has been developed that probe the electronic, vibrational, and chemical fingerprints of defects without damaging the hBN lattice. Optical spectroscopies such as photoluminescence (PL) and cathodoluminescence (CL) can sensitively probe deep-level electronic states associated with vacancy- and impurity-related defects (e.g., V_N, V_B, and C- or O-substitutional sites) [100-102]. Raman and infrared (IR) spectroscopy provides indirect signatures of lattice strain and structural disorder[103,104], while lateral force microscopy (LFM) and conductive atomic force microscopy (CAFM) enable nanoscale detection of atomic defects by detecting variations in frictional or electrical properties, respectively[105]. Furthermore, time-of-flight secondary-ion mass spectrometry (TOF-SIMS) allows nanoscale chemical identification of substitutional elements[106]. When combined with electron microscopy, these complementary approaches can provide correlative insights into the spatial distribution of defects without

damaging the hBN lattice. However, their sensitivity is insufficient to detect low defect concentrations, and these techniques offer low measurement throughput, making large-scale defect analysis difficult.

Atomically clean integration of different elements

Ultimately, constructing vertical structures solely through sequential growth—analogous to conventional thin-film deposition—remains the preferred route. For certain A/hBN/B stacks designed for specific functionalities, direct large-area growth has been demonstrated[54,107]. However, each growth step—synthesizing hBN on material B and depositing material A on hBN—is governed by surface-specific reactions, making broad compatibility across all material combinations difficult to achieve. This challenge is particularly pronounced for hBN, owing to its inherently weak vdW interactions with other materials. Therefore, such possibilities should be tested across various other combinations of heterointerfaces targeting specific functionalities. At the same time, research on controlling interfacial properties via hBN interlayers will continue to advance through the complementary development of both growth and assembly strategies.

Conclusion

This review highlights the use of hBN as an atomically thin interlayer to modulate interfacial interactions. The dependence of these interactions on t_{hBN} can be leveraged to advance the state of the art in electronics and optoelectronics. While significant challenges remain to fully realize the potential of hBN in these fields, continued advancements in synthesis and integration techniques could enable hBN to evolve from a material used for small-scale proof-of-concept demonstrations into a technologically relevant material for large-scale applications.

Acknowledgements

This work was supported by the National R&D Program through the National Research Foundation of Korea (NRF) funded by the Ministry of Science and ICT (2023R1A2C2005427, RS-2023-00234622).

Author Contributions

J.-H. J. and C.-J. K. conceived the outline of the review and wrote the manuscript. All authors have read and approved the final manuscript.

Dielectric constant	**Materials**	**Advantages (as interlayer)**	**Limitations**	**Ref.**
Minimal screening ($\varepsilon < 2$)	Vacuum / Air	Weak dielectric screening	Technical challenges in manufacturing air gaps; Vulnerable to airborne contamination	33
Low-k ($\varepsilon < 4$)	hBN	Atomically flat and chemically inert surface; vdW interfaces with low defect densities; Atomic-scale thickness control;	Lack of standard process for large-scale applications	5,108
Intermediate-k ($4 < \varepsilon < 15$)	SiO_2, Si_3N_4, Al_2O_3, AlN	Atomic-level thickness control via CMOS-compatible process (ex. atomic layer deposition)	Interfacial traps and dangling bonds;	109-112
High-k ($\varepsilon \geq 15$)	HfO_2, ZrO_2		Island-type growth on 2D surfaces limiting atomic-scale thickness control	113,114

Table 1. Comparison of representative dielectric materials used as interlayers.

Optimal hBN thickness (t_{opt})	**Application**	**Related interfacial phenomena**	$t < t_{opt}$	$t > t_{opt}$	**Ref.**
0.7 nm (≈ 2L)	Magnetic tunnel junctions	Spin-polarized tunneling	Metal-metal orbital hybridization → reduced TMR	Exponential tunneling decay → low current & TMR	3,52
0.7–1.0 nm (≈ 2–3 L)	M/S contact (Fermi-level depinning)	Metal wavefunction penetration	Metal-semiconductor orbital hybridization → Fermi-level pinning	Reduced tunneling current → high contact resistance	51
0.7–8 nm (≈ 2–24 L; varies with TMD pair)	Intralayer exciton	Charge tunneling and Förster-type energy transfer	Increasing charge transfer across hBN → PL quenching	Weakened excitonic coupling → reduced PL	66,115 ,116
1–2 nm (≈ 3–6 L)	Remote doping	Coulomb interactions	Insufficient spacing to suppress Coulomb scattering → reduced mobility	Suppressed carrier tunneling → reduced doping efficiency	4,7
~10 L (≈ 3.3 nm)	Gate dielectrics	Coulomb interactions	High leakage currents	Reduced gate efficiency due to low gate capacitance	97
~24 L (≈ 8 nm)	Surface-enhanced Raman scattering	EM near-field enhancement	Metal-analyte orbital hybridization → secondary Raman peaks	Reduced EM field → diminished Raman signal	59

Table 2. Summary of optimal hBN interlayer thickness (t_{opt}) for representative applications.

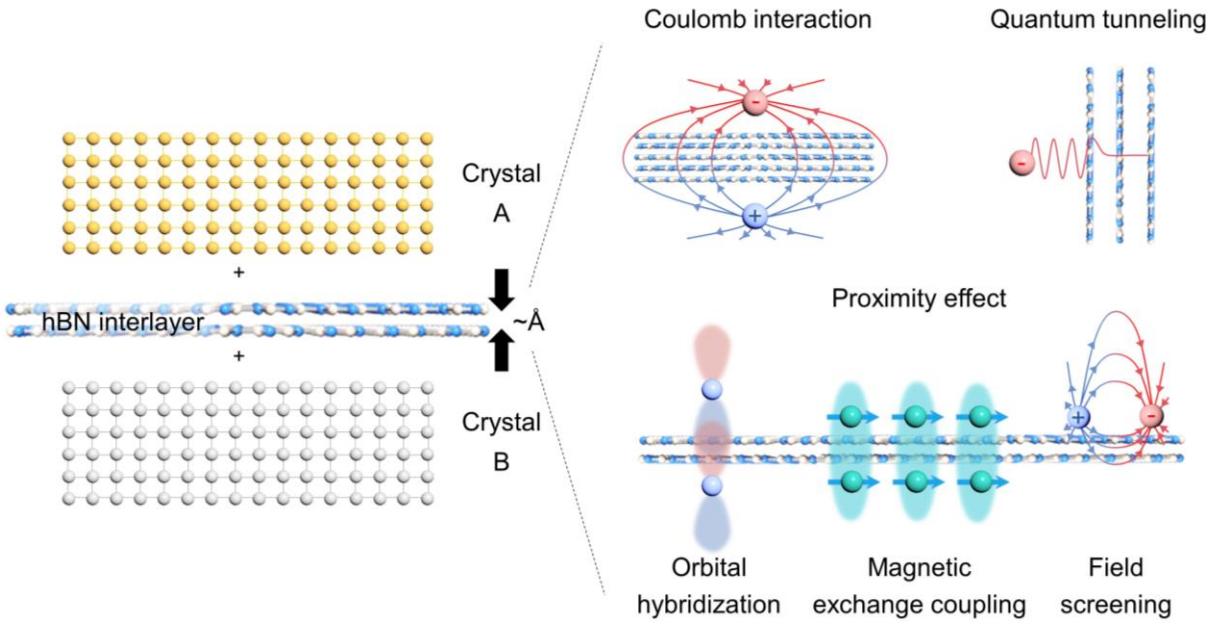

Figure 1. Atomically thin interlayers for programming interfacial states. Schematic of hexagonal boron nitride (hBN) as an atomically thin interlayer for modulating the interaction between two adjacent materials (Crystal A ↔ Crystal B). Distance-dependent modulation of Coulomb interaction and quantum tunneling, as well as proximity effects involving orbital hybridization, magnetic exchange coupling, and field screening.

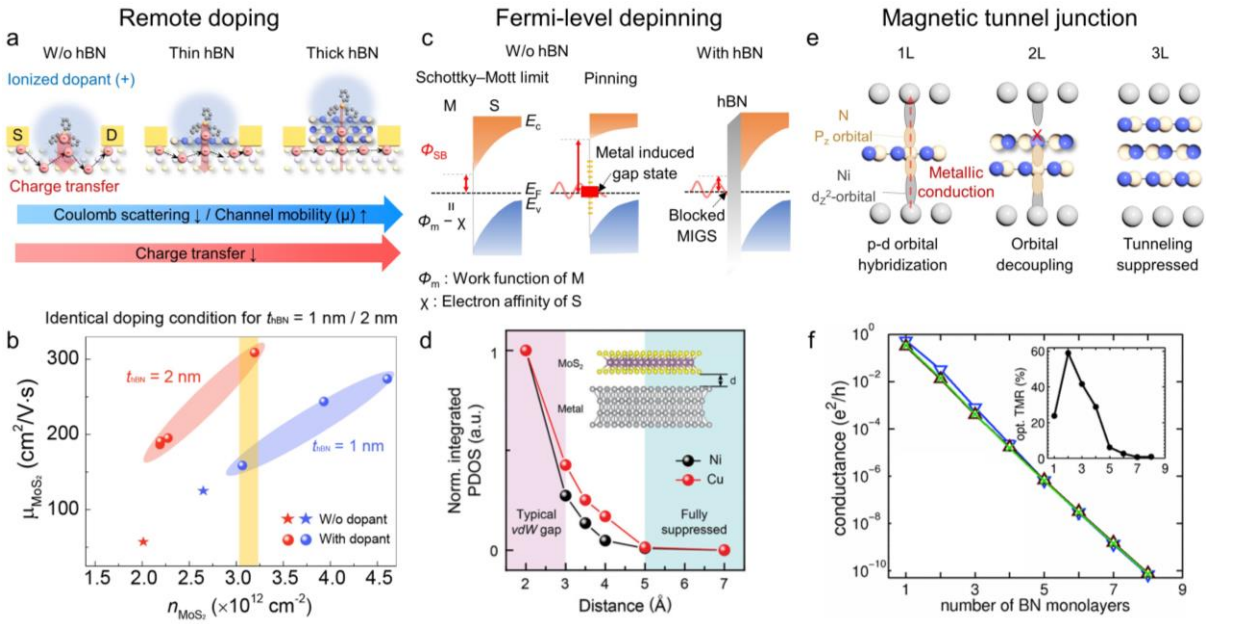

Figure 2. Applications of hBN interlayers for interfacial state modulation in electronics. (a) Schematic of remote doping through an hBN interlayer, showing reduced charge transfer and enhanced suppression of Coulomb scattering with increasing hBN thickness. (S: source electrode; D: drain electrode) (b) Carrier mobility versus carrier concentration (*n*) for remote-doping devices incorporating 1-nm and 2-nm-thick hBN interlayers under identical doping condition. Variation in *n* arises from sample-to-sample variability, but the overall trend shows higher *n* for thinner hBN, accompanied by lower mobility. (c) Energy-band diagrams of metal/semiconductor (M/S) junctions showing the Schottky–Mott limit (no gap states), Fermi-level pinning owing to metal-induced gap states, and depinning with hBN interlayer. (d) Projected density of states (PDOS) in MoS_2 as a function of gap distance between Ni and MoS_2. (e) Schematic of tunneling behavior in Ni/hBN/Ni magnetic tunnel junctions for monolayer, bilayer, and trilayer hBN. (f) Tunneling conductance and tunneling magnetoresistance ratio (TMR) as a function of the number of hBN layers. (b) Adapted under the terms of the Creative Commons Attribution License (CC BY) from Ref. 4. Copyright 2022 American Association for the Advancement of Science. (d) Reprinted under the terms of the Creative Commons Attribution Non-Commercial License (CC BY-NC) from Ref. 51. Copyright 2024 Wiley-VCH. (f) Reprinted with permission from Ref. 52. Copyright 2011 American Physical Society.

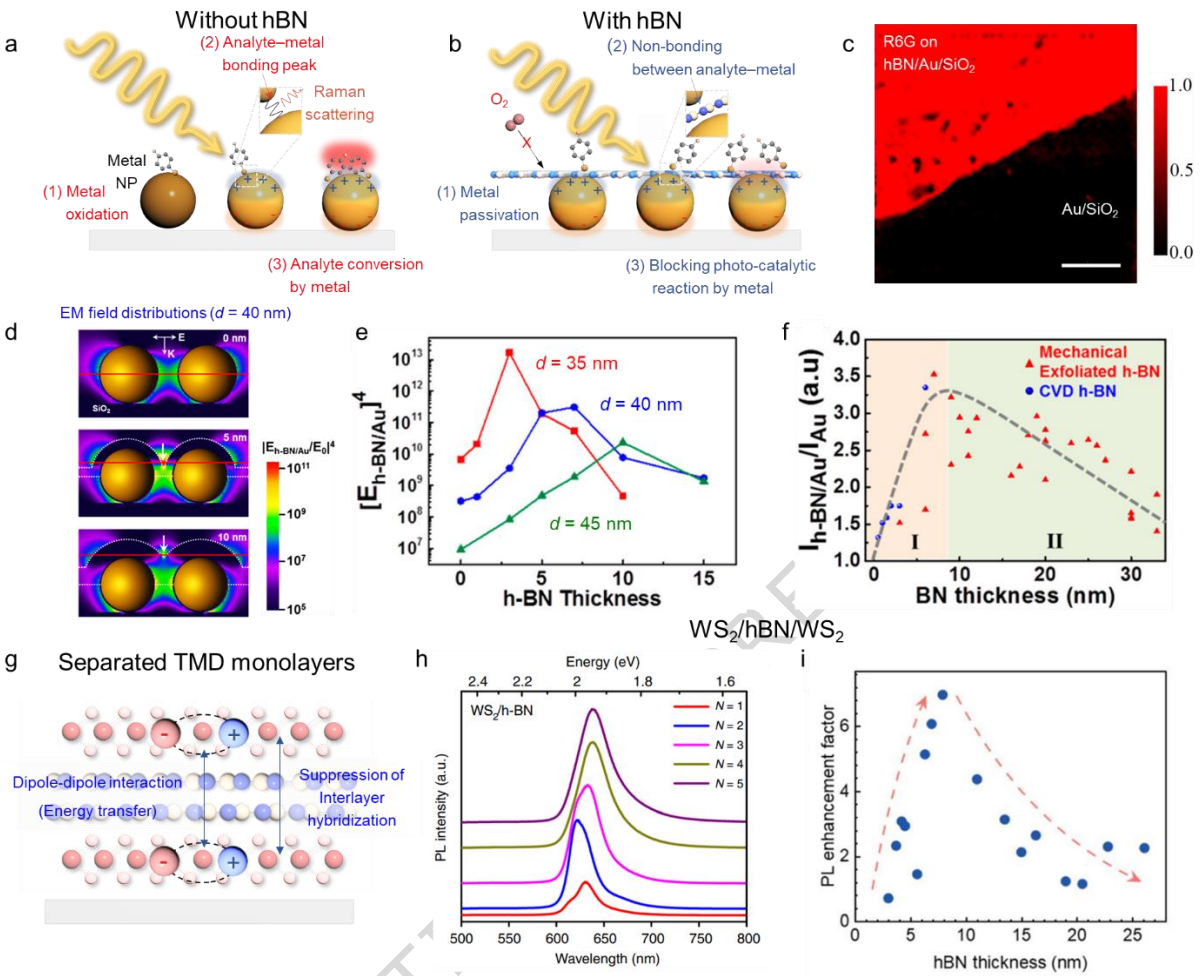

Figure 3. Applications of hBN interlayers in photonics. (a) Schematic of limitations in conventional surface-enhanced Raman scattering (SERS) structures and (b) role of atomically thin hBN interlayer in mitigating these limitations. (c) Raman intensity mapping of R6G molecules on an Au SERS substrate with and without hBN. (d) Cross-sectional electromagnetic (EM) field distributions at varying t_{hBN} (0, 5, 10 nm) for d = 40 nm. (e) Finite-difference time-domain-simulated EM field strength between Au nanoparticles as a function of t_{hBN} and interparticle distance, d. (f) Relative Raman enhancement factor as a function of t_{hBN}. (g) Schematic of an hBN interlayer that increases interlayer distance, suppresses hybridization, and enables Förster-type energy transfer. (h) PL spectra of stacked WS_2/hBN units showing enhanced emission with increasing stack number of hBN. (i) Normalized PL intensity of WS_2/hBN/WS_2 heterostructures as a function of t_{hBN}, exhibiting a nonmonotonic dependence. (c) Adapted with permission from Ref. 61. Copyright 2016 American Chemical Society. (d–f) Adapted with permission from Ref. 59. Copyright 2016 American Chemical Society. (h) Adapted with permission from Ref. 67.

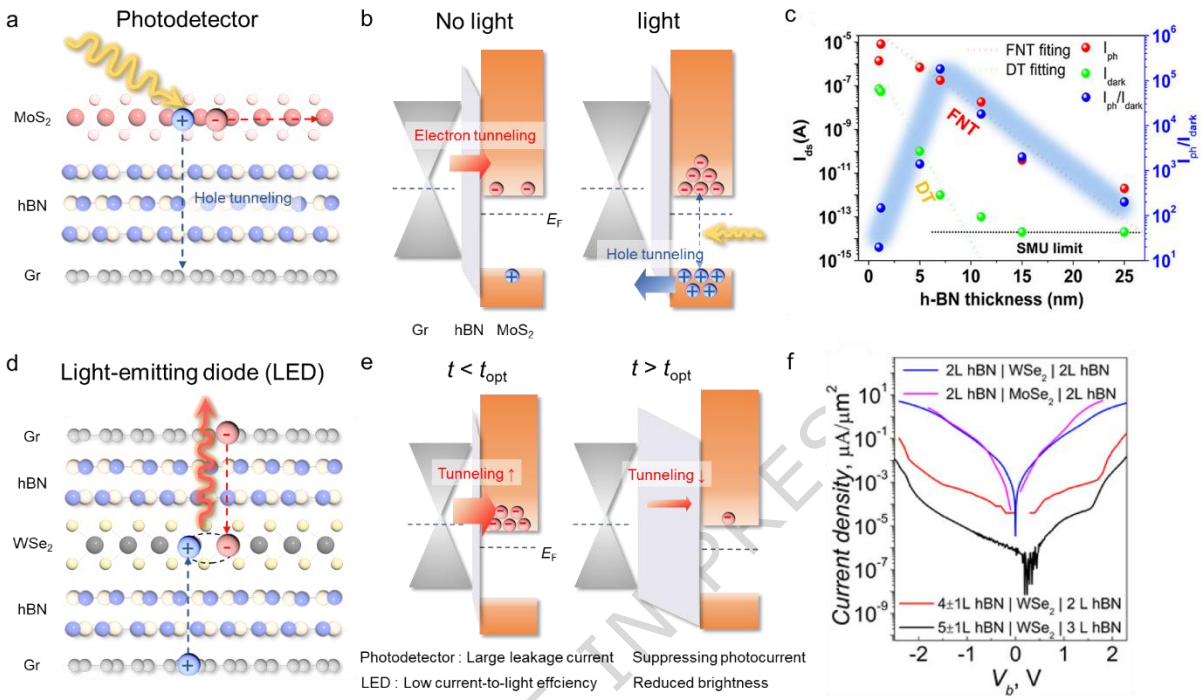

Figure 4. Applications of hBN interlayers in optoelectronics. (a) Schematic of a MoS_2/hBN/graphene photodetector, where photoexcited holes tunnel through the hBN interlayer toward graphene. (b) Energy-band diagram showing asymmetric barrier heights that make hole transport dominant under illumination. (c) Photocurrent and dark-current characteristics as a function of t_{hBN}, demonstrating a trade-off between leakage suppression and photocurrent generation. (d) Schematic of a WSe_2-based light-emitting tunneling device with graphene electrodes. (e) Schematic comparison of thin and thick hBN interlayers. (f) Current–voltage characteristics showing exponential decrease of tunneling current with increasing t_{hBN}. (c) Adapted with permission from Ref. 70. Copyright 2017 American Chemical Society. (f) Adapted with permission from Ref. 57. Copyright 2015 American Chemical Society.

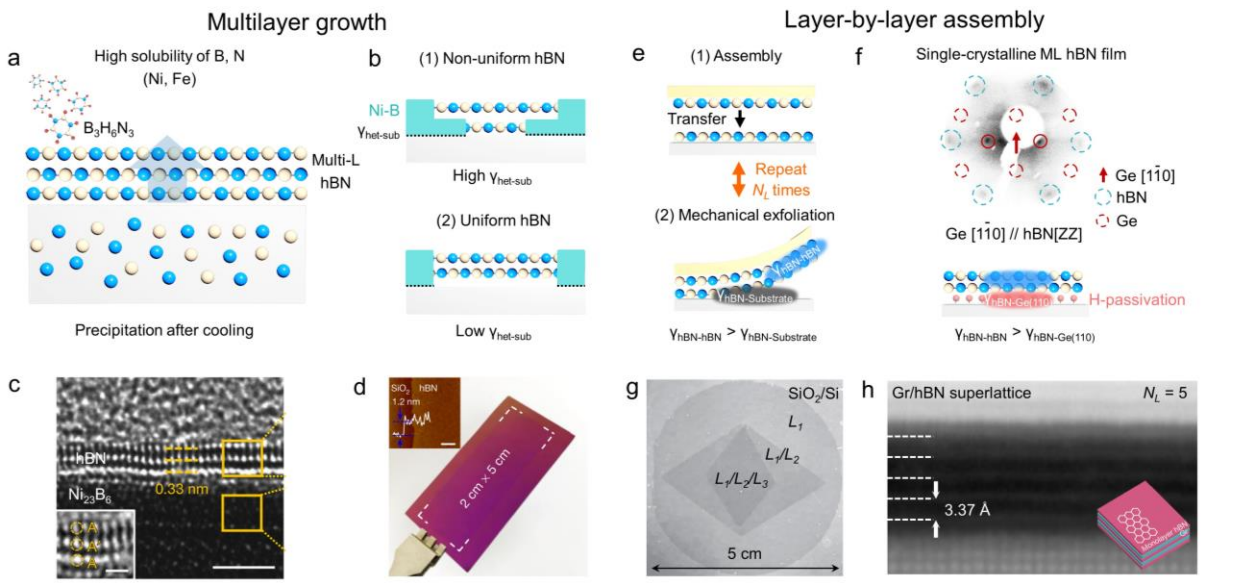

Figure 5. Fabrication of hBN interlayers: epitaxial growth and mechanical assembly. (a) Schematic of multilayer hBN growth via B and N precipitation during cooling of metal substrates after borazine CVD. (b) Comparison between non-synchronized (non-uniform) and synchronized (uniform) multilayer growth. (c) Cross-sectional transmission electron microscopy (TEM) image of epitaxial trilayer hBN. (d) Photograph of wafer-scale (2 cm × 5 cm) trilayer hBN. (e) Schematic of mechanical assembly of chemical vapor deposition–grown hBN. (f) Low-energy electron diffraction pattern of single-crystalline monolayer hBN grown on Ge(110) and schematic of the hydrogen-passivated Ge surface enabling van der Waals-mediated exfoliation. (g) Photograph of wafer-scale assembled epitaxial graphene films grown on Ge(110). (h) Cross-section scanning TEM image of an assembled graphene/hBN superlattice. (c,d) Adapted with permission from Ref. 77. Copyright 2022 Springer Nature. (g,h) Adapted with permission from Ref. 44. Copyright 2022, American Chemical Society.

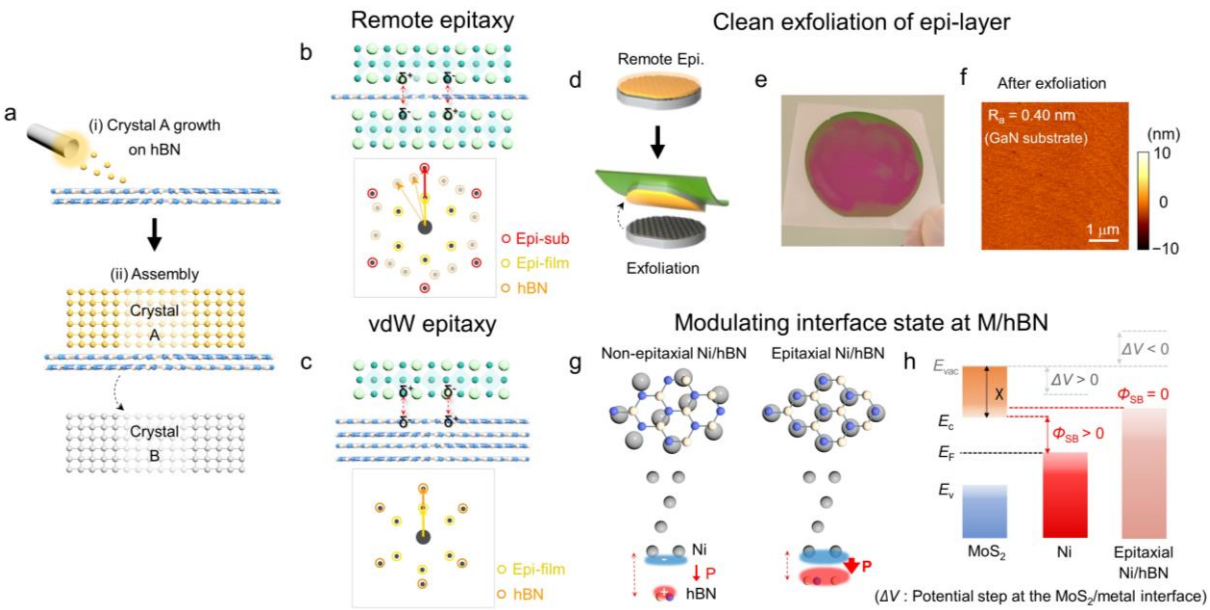

Figure 6. Formations of crystalline membranes via van der Waals (vdW) and remote epitaxy. (a) Schematic of a sandwich heterostructure (A/hBN/B) formed by growing Crystal A on hBN followed by integration with Crystal B. (b) Schematic of remote epitaxy, where the interaction between the substrate and grown film is mediated through atomically thin hBN. The electrostatic potential from the substrate guides the film to align with the crystallographic orientation of the substrate. (c) Schematic of vdW epitaxy, where the epitaxial alignment of the film is governed by vdW interaction with hBN, causing the film to align with the crystallinity of the underlying hBN. (d) Schematic of mechanical exfoliation of epitaxial films grown on hBN. (e) Photograph of a 2-in single-crystalline GaAs membrane exfoliated via hBN-mediated remote epitaxy. (f) Atomic force microscopy image of the substrate after exfoliation, showing minimal roughness (root mean square ~0.40 nm) and clean exfoliation. (g) Atomic configurations of Ni/hBN in non-epitaxial (physisorbed) and epitaxial (chemisorbed) states, showing the difference in interlayer distance and interface dipole formation. (h) Schematic energy band diagrams of MoS_2 with Ni or hBN/Ni interfaces, showing Schottky barrier reduction by a negative potential step ($\Delta V < 0$) induced by the interface dipole at the epitaxial Ni/hBN interface. (d–f) Adapted with permission from Ref. 86. Copyright 2023 Springer Nature.

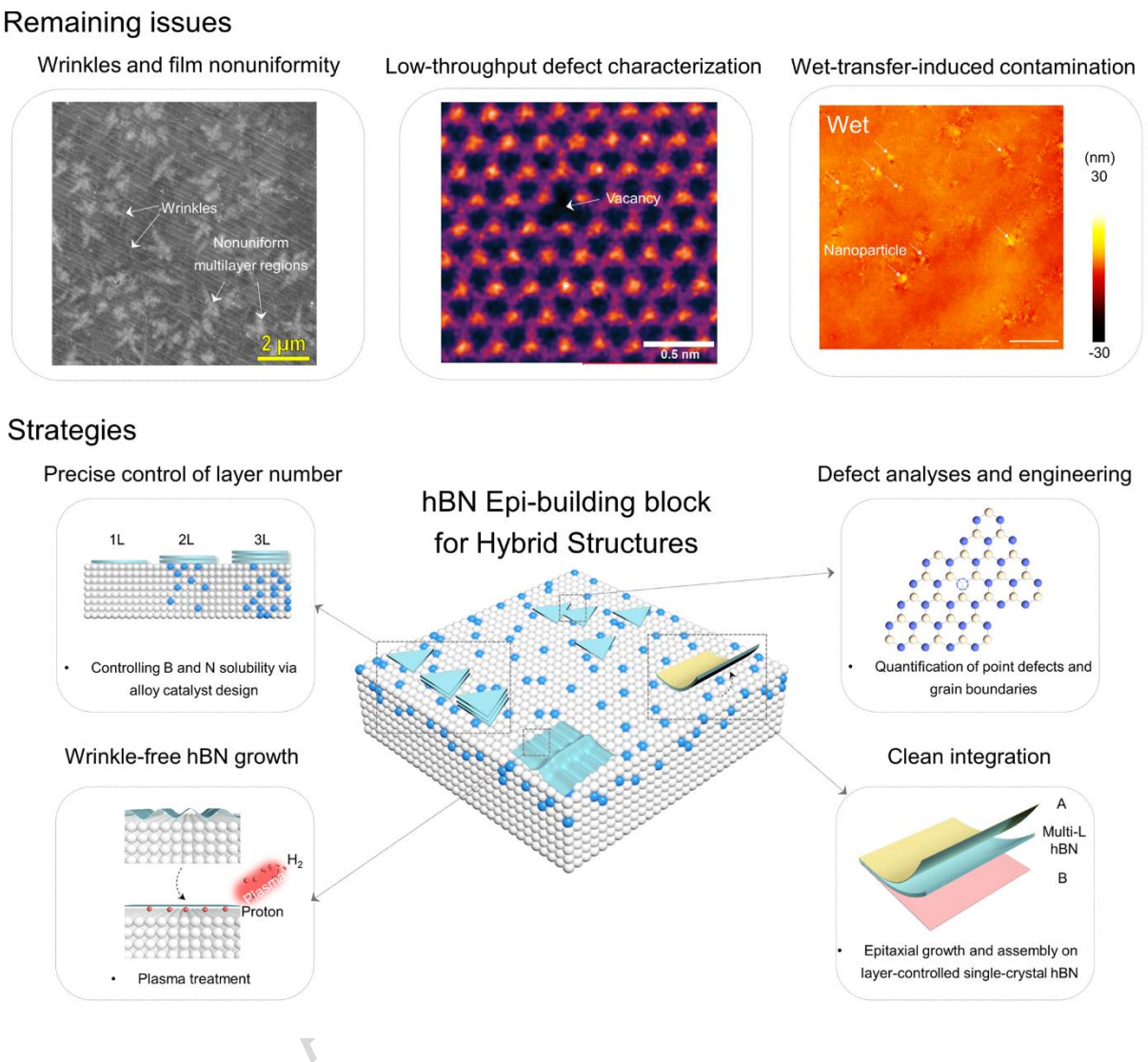

Figure 7. Remaining issues for the growth of hBN interlayers. Atomic-scale layer control, wrinkle suppression, reliable defect analysis, and clean integration are required. The figure also illustrates representative experimental observations[96,117] corresponding to each issue, along with schematic strategies to enable high-quality, scalable hBN synthesis and the integration of crystalline films for applications in advanced electronic and optoelectronic devices. Adapted under the terms of the Creative Commons Attribution License (CC BY) from Ref. 96 and Adapted with permission from Ref. 117. Copyright 2021 Wiley.

References

1 Geim, A. K. & Grigorieva, I. V. Van der Waals heterostructures. *Nature* **499**, 419-425 (2013).

2 Liu, X. & Hersam, M. C. Interface Characterization and Control of 2D Materials and Heterostructures. *Adv. Mater.* **30**, 1801586 (2018).

3 Harfah, H., Wicaksono, Y., Sunnardianto, G. K., Majidi, M. A. & Kusakabe, K. High magnetoresistance of a hexagonal boron nitride–graphene heterostructure-based MTJ through excited-electron transmission. *Nanoscale Adv.* **4**, 117-124 (2022).

4 Jang, J. *et al.* Reduced dopant-induced scattering in remote charge-transfer-doped MoS_2 field-effect transistors. *Sci. Adv.* **8**, eabn3181 (2022).

5 Britnell, L. *et al.* Electron Tunneling through Ultrathin Boron Nitride Crystalline Barriers. *Nano Lett.* **12**, 1707-1710 (2012).

6 Li, J. F. *et al.* Shell-isolated nanoparticle-enhanced Raman spectroscopy. *Nature* **464**, 392-395 (2010).

7 Lee, D. *et al.* Remote modulation doping in van der Waals heterostructure transistors. *Nat. Electron.* **4**, 664-670 (2021).

8 Cai, Q. *et al.* Boron nitride nanosheets improve sensitivity and reusability of surface-enhanced Raman spectroscopy. *Angew. Chem.* **128**, 8545-8549 (2016).

9 Lee, M.-H. *et al.* Two-Dimensional Materials Inserted at the Metal/Semiconductor Interface: Attractive Candidates for Semiconductor Device Contacts. *Nano Lett.* **18**, 4878-4884 (2018).

10 Park, J.-H., Yang, S.-J., Choi, C.-W., Choi, S.-Y. & Kim, C.-J. Pristine graphene insertion at the metal/semiconductor interface to minimize metal-induced gap states. *ACS Appl. Mater. Interfaces* **13**, 22828-22835 (2021).

11 Wang, J. I. *et al.* Hexagonal boron nitride as a low-loss dielectric for superconducting quantum circuits and qubits. *Nat. Mater.* **21**, 398-403 (2022).

12 Mishchenko, A. *et al.* Twist-controlled resonant tunnelling in graphene/boron nitride/graphene heterostructures. *Nat. Nanotechnol.* **9**, 808-813 (2014).

13 Ma, L. *et al.* Strongly correlated excitonic insulator in atomic double layers. *Nature* **598**, 585-589 (2021).

14 Ma, K. Y., Kim, M. & Shin, H. S. Large-Area Hexagonal Boron Nitride Layers by Chemical Vapor Deposition: Growth and Applications for Substrates, Encapsulation, and Membranes. *Acc. Mater. Res.* **3**, 748-760 (2022).

15 Chernikov, A. *et al.* Exciton Binding Energy and Nonhydrogenic Rydberg Series in Monolayer WS_2. *Phys. Rev. Lett.* **113**, 076802 (2014).

16 Raja, A. *et al.* Dielectric disorder in two-dimensional materials. *Nat. Nanotechnol.* **14**, 832-837 (2019).

17 Laturia, A., Van de Put, M. L. & Vandenberghe, W. G. Dielectric properties of hexagonal boron nitride and transition metal dichalcogenides: from monolayer to bulk. *npj 2D Mater. Appl.* **2**, 6 (2018).

18 Keldysh, L. V. Coulomb interaction in thin semiconductor and semimetal films. *JETP Lett.*, **29**, 716 (1979).

19 Berkelbach, T. C., Hybertsen, M. S. & Reichman, D. R. Theory of neutral and charged excitons in monolayer transition metal dichalcogenides. *Phys. Rev. B.* **88**, 045318 (2013).

20 Utama, M. I. B. *et al.* A dielectric-defined lateral heterojunction in a monolayer semiconductor. *Nat. Electron.* **2**, 60-65 (2019).

21 Bai, Y. *et al.* Ultrafast chemical imaging by widefield photothermal sensing of infrared absorption. *Sci. Adv.* **5**, eaav7127 (2019).

22 Raja, A. *et al.* Coulomb engineering of the bandgap and excitons in two-dimensional materials. *Nat. Commun.* **8**, 15251 (2017).

23 Lu, J. M. *et al.* Evidence for two-dimensional Ising superconductivity in gated MoS_2. *Science* **350**, 1353-1357 (2015).

24 Lu, X. *et al.* Superconductors, orbital magnets and correlated states in magic-angle bilayer graphene. *Nature* **574**, 653-657 (2019).

25 van Loon, E. G. C. P. *et al.* Coulomb engineering of two-dimensional Mott materials. *npj 2D Mater. Appl.* **7**, 47 (2023).

26 Cao, Y. *et al.* Correlated insulator behaviour at half-filling in magic-angle graphene superlattices. *Nature* **556**, 80-84 (2018).

27 Florian, M. *et al.* The Dielectric Impact of Layer Distances on Exciton and Trion Binding Energies in van der Waals Heterostructures. *Nano Lett.* **18**, 2725-2732 (2018).

28 He, K. *et al.* Tightly Bound Excitons in Monolayer WSe_2. *Phys. Rev. Lett.* **113**, 026803 (2014).

29 Ghosh, A. *et al.* Advancing excited-state properties of two-dimensional materials using a dielectric-dependent hybrid functional. *Phys. Rev. B.* **112**, 045128 (2025).

30 Lin, Y. *et al.* Dielectric Screening of Excitons and Trions in Single-Layer MoS_2. *Nano Lett.* **14**, 5569-5576 (2014).

31 Ross, J. S. *et al.* Electrically tunable excitonic light-emitting diodes based on monolayer WSe_2 p–n junctions. *Nat. Nanotechnol.* **9**, 268-272 (2014).

32 Ciarrocchi, A., Tagarelli, F., Avsar, A. & Kis, A. Excitonic devices with van der Waals heterostructures: valleytronics meets twistronics. *Nat. Rev. Mater.* **7**, 449-464 (2022).

33 Rhodes, D., Chae, S. H., Ribeiro-Palau, R. & Hone, J. Disorder in van der Waals heterostructures of 2D materials. *Nat. Mater.* **18**, 541-549 (2019).

34 Li, L. H. *et al.* Dielectric Screening in Atomically Thin Boron Nitride Nanosheets. *Nano Lett.* **15**, 218-223 (2015).

35 Zastrow, M. Meet the crystal growers who sparked a revolution in graphene electronics. *Nature* **572**, 429-433 (2019).

36 Dreher, P. *et al.* Proximity Effects on the Charge Density Wave Order and Superconductivity in Single-Layer $NbSe_2$. *ACS Nano* **15**, 19430-19438 (2021).

37 Veyrat, L. *et al.* Helical quantum Hall phase in graphene on $SrTiO_3$. *Science* **367**, 781-786 (2020).

38 Zollner, K., Gmitra, M., Frank, T. & Fabian, J. Theory of proximity-induced exchange coupling in graphene on hBN/(Co, Ni). *Phys. Rev. B.* **94**, 155441 (2016).

39 Jafarpisheh, S. *et al.* Proximity-induced spin-orbit coupling in graphene/$Bi_{1.5}Sb_{0.5}Te_{1.7}Se_{1.3}$ heterostructures. *Phys. Rev. B.* **98**, 241402 (2018).

40 Cohnitz, L., De Martino, A., Häusler, W. & Egger, R. Proximity-induced superconductivity in Landau-quantized graphene monolayers. *Phys. Rev. B.* **96**, 140506 (2017).

41 Island, J. O. *et al.* Spin–orbit-driven band inversion in bilayer graphene by the van der Waals proximity effect. *Nature* **571**, 85-89 (2019).

42 Lin, J.-X. *et al.* Spin-orbit–driven ferromagnetism at half moiré filling in magic-angle twisted bilayer graphene. *Science* **375**, 437-441 (2022).

43 Fan, S. *et al.* Quantum tunneling in two-dimensional van der Waals heterostructures and devices. *Sci. China Mater.* **64**, 2359-2387 (2021).

44 Yang, S.-J. *et al.* Wafer-scale programmed assembly of one-atom-thick crystals. *Nano Lett.* **22**, 1518-1524 (2022).

45 Ko, K. *et al.* Competition between Bipolar Conduction Modes in Extrinsically p-Doped MoS_2: Interaction with Gate Dielectric Matters. *ACS Nano* **19**, 1630-1641 (2025).

46 Liu, X., Choi, M. S., Hwang, E., Yoo, W. J. & Sun, J. Fermi level pinning dependent 2D semiconductor devices: challenges and prospects. *Adv. Mater.* **34**, 2108425 (2022).

47 Liu, Y. *et al.* Approaching the Schottky–Mott limit in van der Waals metal–semiconductor junctions. *Nature* **557**, 696-700 (2018).

48 Kim, C. *et al.* Fermi Level Pinning at Electrical Metal Contacts of Monolayer Molybdenum Dichalcogenides. *ACS Nano* **11**, 1588-1596 (2017).

49 Lan, H.-Y., Tripathi, R., Appenzeller, J. & Chen, Z. Near-Ideal Subthreshold Swing in Scaled 2D Transistors: The Critical Role of Monolayer hBN Passivation. *IEEE Electron Device Lett.* (2024).

50 Wang, J. *et al.* High Mobility MoS_2 transistor with low Schottky barrier contact by using atomic thick h-BN as a tunneling layer. *Adv. Mater.* **28**, 8302-8308 (2016).

51 Kim, Y. H. *et al.* Boltzmann Switching MoS_2 Metal–Semiconductor Field-Effect Transistors Enabled by Monolithic-Oxide-Gapped Metal Gates at the Schottky–Mott Limit. *Adv. Mater.* **36**, 2314274 (2024).

52 Karpan, V. M., Khomyakov, P. A., Giovannetti, G., Starikov, A. A. & Kelly, P. J. Ni (111)|graphene|h-BN junctions as ideal spin injectors. *Phys. Rev. B.* **84**, 153406 (2011).

53 Lee, M.-J. *et al.* Measurement of Exciton and Trion Energies in Multistacked hBN/WS_2 Coupled Quantum Wells for Resonant Tunneling Diodes. *ACS Nano* **14**, 16114-16121 (2020).

54 Xie, J. *et al.* On-chip direct synthesis of boron nitride memristors. *Nat. Nanotechnol.* (2025).

55 Asshoff, P. U. *et al.* Magnetoresistance in Co-hBN-NiFe Tunnel Junctions Enhanced by Resonant Tunneling through Single Defects in Ultrathin hBN Barriers. *Nano Lett.* **18**, 6954-6960 (2018).

56 Tian, J. *et al.* A Josephson junction with h-BN tunnel barrier: observation of low critical current noise. *J. Phys. Condens. Matter.* **33**, 495301 (2021).

57 Withers, F. *et al.* WSe_2 Light-Emitting Tunneling Transistors with Enhanced Brightness at Room Temperature. *Nano Lett.* **15**, 8223-8228 (2015).

58 Lorchat, E. *et al.* Filtering the photoluminescence spectra of atomically thin semiconductors with graphene. *Nat. Nanotechnol.* **15**, 283-288 (2020).

59 Kim, G. *et al.* Hexagonal boron nitride/Au substrate for manipulating surface plasmon and enhancing capability of surface-enhanced Raman spectroscopy. *ACS Nano* **10**, 11156-11162 (2016).

60 Guselnikova, O. *et al.* New trends in nanoarchitectured SERS substrates: nanospaces, 2D materials, and organic heterostructures. *Small* **18**, 2107182 (2022).

61 Cai, Q. *et al.* Boron nitride nanosheet-veiled gold nanoparticles for surface-enhanced Raman scattering. *ACS Appl. Mater. Interfaces* **8**, 15630-15636 (2016).

62 Caldwell, J. D. *et al.* Photonics with hexagonal boron nitride. *Nat. Rev. Mater.* **4**, 552-567 (2019).

63 Splendiani, A. *et al.* Emerging Photoluminescence in Monolayer MoS_2. *Nano Lett.* **10**, 1271-1275 (2010).

64 Wang, C. *et al.* Monolayer atomic crystal molecular superlattices. *Nature* **555**, 231-236 (2018).

65 Zhou, J. *et al.* Layered Intercalation Materials. *Adv. Mater.* **33**, 2004557 (2021).

66 Xu, Z. *et al.* Synergistic effects of charge transfer, energy transfer and cavity interference on the exciton emission in WS_2/hBN/WS_2 heterostructures. *Nanoscale* **17**, 18889-18899 (2025).

67 Kumar, P. *et al.* Light–matter coupling in large-area van der Waals superlattices. *Nature Nanotechnology* **17**, 182-189 (2022).

68 Zhou, H. *et al.* Controlling Exciton and Valley Dynamics in Two-Dimensional Heterostructures with Atomically Precise Interlayer Proximity. *ACS Nano* **14**, 4618-4625 (2020).

69 Fang, H. *et al.* Strong interlayer coupling in van der Waals heterostructures built from single-layer chalcogenides. *Proc. Natl. Acad. Sci.* **111**, 6198-6202 (2014).

70 Vu, Q. A. *et al.* Tuning Carrier Tunneling in van der Waals Heterostructures for Ultrahigh Detectivity. *Nano Lett.* **17**, 453-459 (2017).

71 Islam, M. S. *et al.* Growth mechanisms of monolayer hexagonal boron nitride (h-BN) on metal surfaces: theoretical perspectives. *Nanoscale Advances* **5**, 4041-4064 (2023).

72 Page, R. *et al.* Rotationally aligned hexagonal boron nitride on sapphire by high-temperature molecular beam epitaxy. *Phys. Rev. Mater.* **3**, 064001 (2019).

73 Cho, Y.-J. *et al.* Hexagonal Boron Nitride Tunnel Barriers Grown on Graphite by High Temperature Molecular Beam Epitaxy. *Sci. Rep.* **6**, 34474 (2016).

74 Moon, S. *et al.* Metal-organic chemical vapor deposition of hexagonal boron nitride: from high-quality growth to functional engineering. *2D Mater.* **12**, 042006 (2025).

75 Kobayashi, Y., Kumakura, K., Akasaka, T. & Makimoto, T. Layered boron nitride as a release layer for mechanical transfer of GaN-based devices. *Nature* **484**, 223-227 (2012).

76 Sharma, S. *et al.* The Influence of Carbon on Polytype and Growth Stability of Epitaxial Hexagonal Boron Nitride Films. *Adv. Mater. Interfaces.* **11**, 2400091 (2024).

77 Ma, K. Y. *et al.* Epitaxial single-crystal hexagonal boron nitride multilayers on Ni (111). *Nature* **606**, 88-93 (2022).

78 Kim, S. M. *et al.* Synthesis of large-area multilayer hexagonal boron nitride for high material performance. *Nat. Commun.* **6**, 8662 (2015).

79 Shi, Z. *et al.* Vapor–liquid–solid growth of large-area multilayer hexagonal boron nitride on dielectric substrates. *Nat. Commun.* **11**, 849 (2020).

80 Zhang, L., Kong, X., Dong, J. & Ding, F. A mechanism for thickness-controllable single crystalline 2D materials growth. *Sci. Bull.* **68**, 2936-2944 (2023).

81 Jung, J. H. *et al.* Step-Directed Epitaxy of Unidirectional Hexagonal Boron Nitride on Vicinal Ge (110). *Small Struct.* **5**, 2400297 (2024).

82 Liu, Y., Huang, Y. & Duan, X. Van der Waals integration before and beyond two-dimensional materials. *Nature* **567**, 323-333 (2019).

83 Pham, P. V. *et al.* Transfer of 2D Films: From Imperfection to Perfection. *ACS Nano* **18**, 14841-14876 (2024).

84 Kim, H. *et al.* Remote epitaxy. *Nat. Rev. Methods. Primers* **2**, 40 (2022).

85 Kong, W. *et al.* Polarity governs atomic interaction through two-dimensional materials. *Nat. Mater.* **17**, 999-1004 (2018).

86 Kim, H. *et al.* High-throughput manufacturing of epitaxial membranes from a single wafer by 2D materials-based layer transfer process. *Nat. Nanotechnol.* **18**, 464-470 (2023).

87 Farmanbar, M. & Brocks, G. Ohmic contacts to 2D semiconductors through van der Waals bonding. *Adv. Electron. Mater.* **2**, 1500405 (2016).

88 Farmanbar, M. & Brocks, G. Controlling the Schottky barrier at MoS_2/metal contacts by inserting a BN monolayer. *Phys. Rev. B.* **91**, 161304 (2015).

89 Wang, G., Yang, P., Moody, N. A. & Batista, E. R. Overcoming the quantum efficiency-lifetime tradeoff of photocathodes by coating with atomically thin two-dimensional nanomaterials. *npj 2D Mater. Appl.* **2**, 17 (2018).

90 Park, J.-H. *et al.* Reduction of Hole Carriers by van der Waals Contact for Enhanced Photoluminescence Quantum Yield in Two-Dimensional Tin Halide Perovskite. *ACS Energy Letters* **8**, 3536-3544 (2023).

91 Nguyen, V. L. *et al.* Layer-controlled single-crystalline graphene film with stacking order via Cu–Si alloy formation. *Nat. Nanotechnol.* **15**, 861-867 (2020).

92 Zhao, C., Shan, L., Sun, R., Wang, X. & Ding, F. Wrinkle formation in synthesized graphene and 2D materials. *Mater. Today* (2024).

93 Wang, Y. *et al.* Ultraflat single-crystal hexagonal boron nitride for wafer-scale integration of a 2D-compatible high-κ metal gate. *Nat. Mater.* **23**, 1495-1501 (2024).

94 Yuan, G. *et al.* Proton-assisted growth of ultra-flat graphene films. *Nature* **577**, 204-208 (2020).

95 Hu, S. *et al.* Proton transport through one-atom-thick crystals. *Nature* **516**, 227-230 (2014). https://doi.org:10.1038/nature14015

96 Yuan, Y. *et al.* On the quality of commercial chemical vapour deposited hexagonal boron nitride. *Nat. Commun.* **15**, 4518 (2024).

97 Knobloch, T. *et al.* The performance limits of hexagonal boron nitride as an insulator for scaled CMOS devices based on two-dimensional materials. *Nat. Electron.* **4**, 98-108 (2021).

98 Chubarov, M. *et al.* Wafer-scale epitaxial growth of unidirectional WS_2 monolayers on sapphire. *ACS Nano* **15**, 2532-2541 (2021).

99 Suenaga, K., Kobayashi, H. & Koshino, M. Core-level spectroscopy of point defects in single layer h-BN. *Phys. Rev. Lett.* **108**, 075501 (2012).

100 Qiu, Z. *et al.* Atomic and Electronic Structure of Defects in hBN: Enhancing Single-Defect Functionalities. *ACS Nano* **18**, 24035-24043 (2024).

101 Tang, T. W. *et al.* Structured-Defect Engineering of Hexagonal Boron Nitride for Identified Visible Single-Photon Emitters. *ACS Nano* **19**, 8509-8519 (2025).

102 Sankar, S. *et al.* Optical Properties of Low-Defect Large-Area Hexagonal Boron Nitride for Quantum Applications. *Phys. Status Solidi RRL* **18**, 2400034 (2024).

103 Okonai, T. *et al.* Anomalous Raman signals in multilayer hexagonal boron nitride grown by chemical vapour deposition on metal foil catalysts. *Nanoscale Adv.* (2025).

104 Lyu, B. *et al.* Phonon Polariton-assisted Infrared Nanoimaging of Local Strain in Hexagonal Boron Nitride. *Nano Lett.* **19**, 1982-1989 (2019).

105 Yang, Y. *et al.* Atomic Defect Quantification by Lateral Force Microscopy. *ACS Nano* **18**, 6887-6895 (2024).

106 Ismach, A. *et al.* Carbon-assisted chemical vapor deposition of hexagonal boron nitride. *2D Materials* **4**, 025117 (2017).

107 Chen, M. *et al.* Ultrawide-bandwidth boron nitride photonic memristors. *Nat. Nanotechnol.* (2025).

108 Lee, G.-H. *et al.* Electron tunneling through atomically flat and ultrathin hexagonal boron nitride. *Appl. Phys. Lett.* **99** (2011).

109 Kaushik, N. *et al.* Reversible hysteresis inversion in MoS_2 field effect transistors. *npj 2D Mater. Appl.* **1**, 34 (2017).

110 Hwang, S. *et al.* A facile approach towards Wrinkle-Free transfer of 2D-MoS2 films via hydrophilic Si_3N_4 substrate. *Appl. Surf. Sci.* **604**, 154523 (2022).

111 Zhao, P. *et al.* Understanding the Impact of Annealing on Interface and Border Traps in the $Cr/HfO_2/Al_2O_3/MoS_2$ System. *ACS Appl. Electron. Mater.* **1**, 1372-1377 (2019).

112 Qian, Q. *et al.* Improved Gate Dielectric Deposition and Enhanced Electrical Stability for Single-Layer MoS_2 MOSFET with an AlN Interfacial Layer. *Sci. Rep.* **6**, 27676 (2016).

113 McDonnell, S. *et al.* HfO_2 on MoS_2 by Atomic Layer Deposition: Adsorption Mechanisms and Thickness Scalability. *ACS Nano* **7**, 10354-10361 (2013).

114 Yan, H. *et al.* A clean van der Waals interface between the high-k dielectric zirconium oxide and two-dimensional molybdenum disulfide. *Nat. Electron.* **8**, 906-912 (2025).

115 Xu, W. *et al.* Determining the Optimized Interlayer Separation Distance in Vertical Stacked 2D WS_2:hBN:MoS_2 Heterostructures for Exciton Energy Transfer. *Small* **14**, 1703727 (2018).

116 Xu, W. *et al.* Controlling Photoluminescence Enhancement and Energy Transfer in WS_2:hBN:WS_2 Vertical Stacks by Precise Interlayer Distances. *Small* **16**, 1905985

117 Park, H. *et al.* Atomically Precise Control of Carbon Insertion into hBN Monolayer Point Vacancies using a Focused Electron Beam Guide. *Small* **17**, 2100693 (2021).